This article has been accepted for publication in a future issue of this journal, but has not been fully edited. Content may change prior to final publication. Citation information: DOI 10.1109/TVT.2017.2678532, IEEE Transactions on Vehicular Technology

An Isolated/Bidirectional PWM Resonant Converter for V2G(H) EV On-Board Charger

Byung-Kwon Lee, Jong-Pil Kim, Sam-Gyun Kim, and Jun-Young Lee, *Member, IEEE*

***Abstract*— This paper suggests another candidate for isolated/bidirectional DC/DC converter in electric vehicle (EV) on-board charger (OBC) based on PWM resonant converter (RC). The PWM-RC has good switching characteristics but it is not adequate for bidirectional applications because it is always operated under 'buck type' operation regardless of power flow directions. This problem can be solved by structure change method, which increases the converter gain into double. Also, additional technique to increase the converter gain during discharging operation is suggested by analysis of the gain characteristics. The feasibility of bidirectional PWM-RC is verified with a 6.6kW prototype charger.**

***Index Terms*— Battery charger, Resonant converter, Bidirectional converter**

I. Introduction

INCREASE of transportation energy usage and worries of air pollution have expedited vehicle electrification. Since electrical vehicles (EVs) have a high potential to reduce emission of greenhouse gasses and gasoline usage, they are expected to become commonly used all around the world in the near future as green transportation system. EVs use a high capacity battery pack that can be recharged through power grid so that they provide an opportunity to employ vehicle-to-grid (house) (V2G(H)) technology. V2G(H) technology makes EV an energy storage device by providing the battery power to the grid or the local loads. A large number of EVs interconnected with the utility will be an alternative solution to stabilize the intermittent renewable energy sources and emergency power supply [1~4]. In order for EVs to be operated with V2G(H) function, bidirectional on-board charger (OBC) that regulates bidirectional power flow is essential equipment. Conventional EV bidirectional OBCs are comprised of bidirectional AC/DC converter for harmonic regulation and grid-tied operation followed by isolated/bidirectional DC/DC converter for battery charging and discharging operations. For AC/DC converter, H-bridge-based converters such as single-phase half-bride, single-phase full-bride, and three-phase full-bride converters are generally used for grid-connected converters and multilevel topologies are also considered in high power chargers [5~7]. Recently, many efforts have been focused on improvement of the efficiency in conventional AC/DC converter structures and good efficiencies over 97~99% have been reported based on new devices such as silicon carbide (SiC) devices [8-14]. It means that there are many solutions available for improvement of power density and efficiency in grid-tied converter of bidirectional OBCs. Accordingly, overall efficiency and size are strongly affected by bidirectional DC/DC stage as a result. To be able to be used for battery charger and improve OBC efficiency that seriously affects mileage, DC/DC stage should meet several requirements such as wide output voltage regulation, low electrical stresses, no snubber circuitry, low circulating current, and good switching condition. Above all, the critical requirement for bidirectional application is whether buck/boost operation is available or not [15, 16]. Conventional isolated/bidirectional PWM converters have common structure with voltage-fed side comprised of voltage source and high frequency (HF) inverter and current-fed side comprised of inductor and HF inverter. This structure meets the critical requirement of buck/boost operation but HF inverter in current-fed side suffers from heavy voltage stress caused by transformer leakage inductance [16, 18]. Moreover, this problem becomes worse in high voltage applications such as OBC, which makes it impossible to use high frequency switches of MOSFET even snubber circuitry is adopted. It is a major obstacle for size reduction and efficiency improvement of OBC [17-20]. For high voltage isolated/bidirectional converters, symmetrical structure that has voltage-fed input and voltage-fed output is very advantageous. This structure includes resonant converters and dual-active-bridge (DAB) converter. Among them, DAB is more adequate for bidirectional applications because it has the 'buck/boost type' operation for bidirectional power transfer, the ability to accommodate a wide range of voltage levels, and a high power capability [21]. However, the conventional DAB converter has large reactive current flows, which provides electrical stress on its switching elements and

Manuscript received September 08, 2016; revised December 12, 2016; revised January 26, 2017; accepted February 23, 2017.

This work was supported by Hyundai Motor Company and the Korea Evaluation Institute of Industrial Technology (KEIT) grant funded by the Korea government Ministry of Trade Industry and Energy (No. 10062459).

Jun-Young Lee and Byung-Kwon Lee are with the Department of Electrical Engineering, Myongji University, 116, Myongji-ro, Cheoin-Gu, Yongin-si, Gyeongg-do, 17058, Korea (E-mail: pdpljy@mju.ac.kr, bklovewjh@naver.com)

Jong-Pil Kim and Sam-Gyun Kim are with the Advanced Eco-Vehicle Team, Hyundai Motor Company, 150 Hyundaiyeonguso-ro, Namyang-eup, Hwasung-si, Gyeonggi-do, 18278, Korea(E-mail: jp1120.kim@hyundai.com, samgkim@hyundai.com)

This article has been accepted for publication in a future issue of this journal, but has not been fully edited. Content may change prior to final publication. Citation information: DOI 10.1109/TVT.2017.2678532, IEEE Transactions on Vehicular Technology

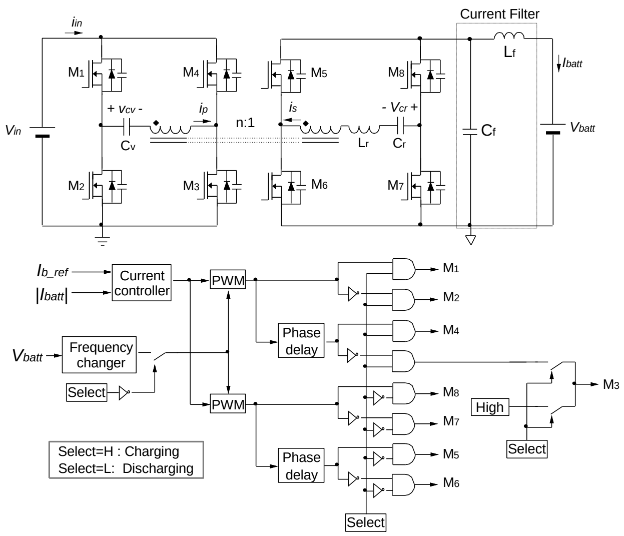

Fig. 1 Proposed circuit and its control block diagram

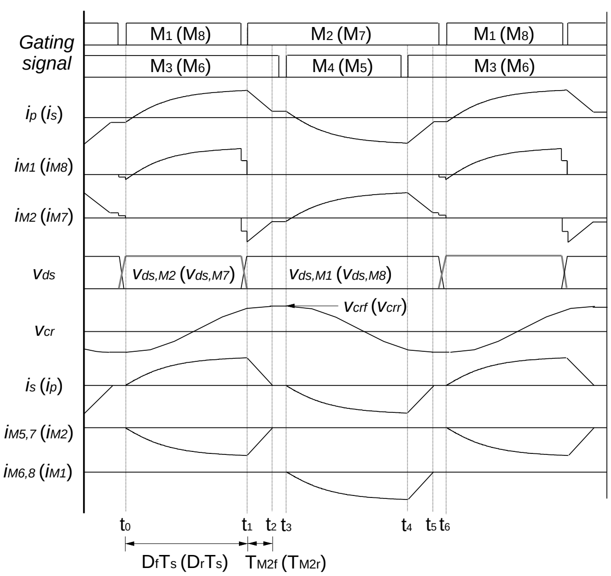

Fig. 2 Key waveforms for mode analysis of charging and discharging operations (symbols in parentheses: discharging operation)

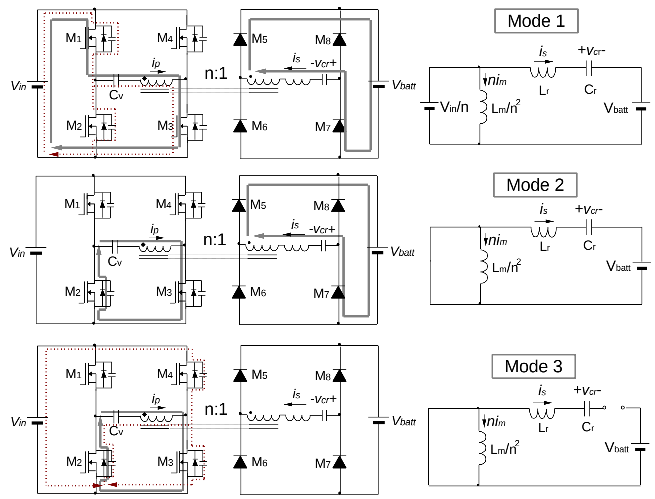

Fig. 3 Mode diagrams and their equivalent circuits in charging operation

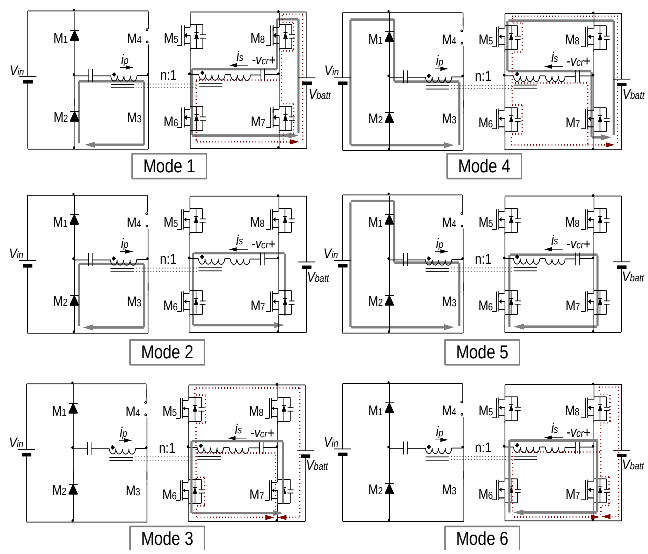

Fig. 4 Mode diagrams in discharging operation

increase of power losses [22]. To solve these problems and improve the efficiency, various control methods and applications of new semiconductor devices have been suggested [24-26].

In this paper, another candidate for isolated/bidirectional OBC is proposed using PWM resonant converter (RC). The PWM-RC has constant frequency PWM control and good switching characteristics. By proper design of the resonant tank, upper switches can be operated with zero-voltage turn-on, and other switching devices including bottom switches and output rectifier can have zero-voltage turn-on and zero-current turn-off [27]. This PWM-RC can be modified for bidirectional power flow by replacing rectifier with switches. However, the bidirectional PWM-RC is always operated with 'buck type' operation regardless of power flow directions so that it is difficult to have discharging operation over entire battery voltage range. This defect can be overcome by structure change method that changes the rectifier structure to increase the voltage gain into double. Also, an additional technique to increase the converter gain during discharging operation is suggested by analysis of the gain characteristics.

II. Analysis of the Proposed Converter

A. *Description of the proposed converter*

Fig. 1 is the schematic diagram of the proposed bidirectional DC/DC converter. The converter has symmetrical structure like DAB converter. It has 8 switches for charging or discharging operations. Resonant tank comprised of resonant capacitor C_r and resonant inductor L_r is located on the secondary side for resonant PWM operation and the capacitor C_v located on the primary side is for voltage-doubling operation. Since the converter is controlled only by PWM different from conventional resonant converters, efficiency degradation due to excessive high switching frequency, and audible noise or no-load regulation problems due to excessive low switching frequency can be avoided [27]. The proposed bidirectional charger keeps structural advantages similar to DAB converter such as low voltage stress of switches and absorption of transformer leakage inductance by circuit parameter. Different from DAB converter, the proposed converter operates with 'buck type' regardless of power flow direction, which makes it difficult for the converter to form bidirectional power flow. To solve this problem, the proposed converter adopts voltage-doubler rectification structure in case of discharging operation, which increases the voltage gain into double [28]. This function can be implemented by keeping M_3 on conducting-state during discharging operation. The operation will be explained in the next section.

B. Mode analysis of charging operation

In charging operation, the power flow is controlled by M_1~M_4 and body diodes of M_5~M_8 are used for full-bridge rectifier. In this case, C_v is used for DC-coupling capacitor so that it does not affect the operation if C_v has a sufficiently large value. Fig. 2 is key waveforms for mode analysis of charging and discharging operations. In this figure, symbols in parentheses are for discharging operation. Mode diagrams and their equivalent circuits in charging operation are in Fig. 3. Before analysis, it is assumed that all switching devices are ideal without drain-source capacitance C_{ds} and the resonant capacitor voltage v_{cr} does not exceed the battery voltage V_{batt}. Also, M_3 is on conducting-state before mode 1.

Mode 1 ($t_0 \le t < t_1$): When M_1 is turn on at t_0, the primary current i_p flows through M_1, M_3, and the transformer primary side. The secondary current i_s increases from zero through L_r, C_r, body diodes of M_5 and M_7, and transformer secondary side. From the equivalent circuit of mode 1, v_{cr} and i_s can be derived as

$$v_{cr}(t)=\left(\frac{V_{in}}{n}-V_{batt}\right)-\left(\frac{V_{in}}{n}+V_{crf}-V_{batt}\right)\cos\omega_r(t-t_0) \quad (1)$$

$$i_s(t)=\frac{1}{Z_r}\left(\frac{V_{in}}{n}+V_{crf}-V_{batt}\right)\sin\omega_r(t-t_0) \quad (2)$$

where $\omega_r=1/(L_rC_r)^{0.5}$ and $Z_r=(L_r/C_r)^{0.5}$. V_{crf} is the peak voltage of v_{cr} in charging operation and its expression is as shown in eq. (8). The primary current i_p is the sum of i_s referred to the primary side and the magnetizing current i_m. When M_1 is turned off, the primary current is used to charge and discharge C_{ds}'s of M_1 and M_2. If C_{ds} of M_2 is completely discharged before the end of mode 1, zero-voltage-switching (ZVS) of M_2 can be accomplished. Fortunately, ZVS condition of M_2 is easily satisfied because the peak value of i_p is used for ZVS. This operation is depicted with dotted line in mode 1 diagram in Fig. 3

Mode 2 ($t_1 \le t < t_2$): When M_2 is turned on, mode 2 begins. The primary current i_p flows through M_3, the body diode of M_2, and the transformer primary side. The secondary current i_s keeps same current path with the previous modes until i_s is decreased to zero. From the equivalent circuit of mode 2, v_{cr} and i_s can be expressed as the following equations:

$$v_{cr}(t)=-V_{batt}+\left(v_{cr}(t_1)+V_{batt}\right)\cos\omega_r(t-t_1)+Z_r i_{Lr}(t_1)\sin\omega_r(t-t_1) \quad (3)$$

$$i_s(t)=-\frac{1}{Z_r}\left(v_{cr}(t_1)+V_{batt}\right)\sin\omega_r(t-t_1)+i_{Lr}(t_1)\cos\omega_r(t-t_2) \quad (4)$$

With the assumption that dead-times between gate signals of upper and lower switches are short enough to be neglected, $i_{Lr}(t_1)$ and $v_{cr}(t_1)$ can be found from eqs. (1) and (2) as follows:

$$v_{cr}(t_1)\cong v_{cr}(D_fT_s)=\left(\frac{V_{in}}{n}-V_{batt}\right)-\left(\frac{V_{in}}{n}+V_{crf}-V_{batt}\right)\cos\omega_r D_f T_s \quad (5)$$

$$i_s(t_1)\cong i_s(D_fT_s)=\frac{1}{Z_r}\left(\frac{V_{in}}{n}+V_{crf}-V_{batt}\right)\sin\omega_r D_f T_s \quad (6)$$

Where, D_f is the duty-ratio of M_1 (or M_4) in charging operation. From eqs. (4), (5), and (6), the duration of mode 2, T_{M2f}, can be derived as

$$T_{M2f}=\frac{1}{\omega_r}\tan^{-1}\left(-\frac{\left(\frac{V_{in}}{n}+V_{crf}-V_{batt}\right)\sin\omega_r D_f T_s}{-\frac{V_{in}}{n}+\left(\frac{V_{in}}{n}+V_{crf}-V_{batt}\right)\cos\omega_r D_f T_s}\right) \quad (7)$$

Mode 3 ($t_2 \le t < t_3$): After mode 2, only the magnetizing current i_m circulates through M_3 and the body diode of M_2. During mode 3, the resonant capacitor voltage v_{cr} is kept as $v_{cr}(t_2)$ which is the peak value of the resonant capacitor defined by V_{crf}. From eqs. (3) and (7), V_{crf} can be derived as follows:

$$v_{cr}(t_2)\cong\frac{\frac{V_{in}}{n}\left(\frac{V_{in}}{n}-V_{batt}\right)\left(1-\cos\omega_r D_f T_s\right)}{2V_{batt}-\frac{V_{in}}{n}\left(1-\cos\omega_r D_f T_s\right)}\equiv V_{crf} \quad (8)$$

V_{crf} should not exceed V_{batt} to guarantee the normal operation by preventing body diodes of M_5 and M_7 from conducting abnormally. Referring to key waveform in Fig. 2 and mode diagram in Fig. 3, only the peak magnetizing current is used to charge and discharge C_{ds}'s of M_3 and M_4. If C_{ds} of M_4 is completely discharged before the end of mode 3, ZVS of M_4 can be accomplished. Different from ZVS condition of M_2, ZVS of M_4 is not easy because only the peak value of the magnetizing current is used for ZVS and it is affected by load condition. The

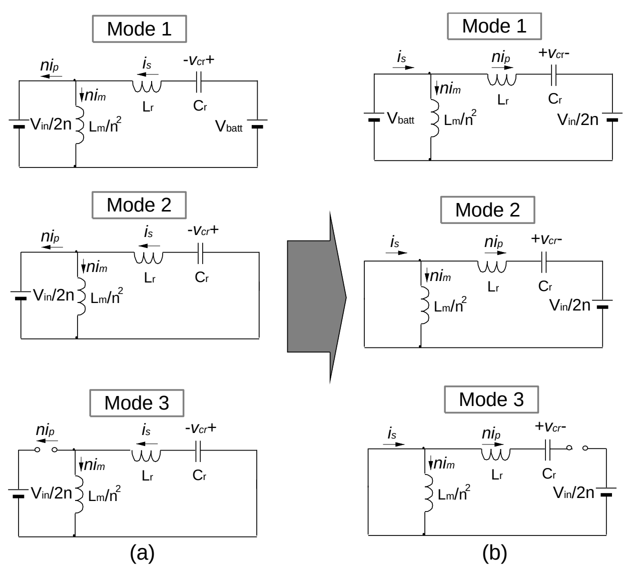

Fig. 5 Equivalent circuits of modes 1~3(a) and their modifications (b)

This article has been accepted for publication in a future issue of this journal, but has not been fully edited. Content may change prior to final publication. Citation information: DOI 10.1109/TVT.2017.2678532, IEEE Transactions on Vehicular Technology

operation of the next half-cycle comprised of modes 4~6 is same as that of the first half-cycle.

C. Mode analysis of discharging operation

The power flow is controlled by M_5~M_8 in discharging operation. To increase the voltage gain, the rectifier using body diodes of M_1 and M_2 is operated as voltage-doubler rectifier by keeping M_3 on conducting-state. The capacitor C_v is used for charge-pump capacitor and the capacitor voltage v_{cv} becomes $V_{in}/2$. Mode diagrams and their equivalent circuits are as shown in Figs. 4 and 5(a). Assuming that the impedance of the magnetizing inductance referred to the transformer secondary side, $\omega_s L_m/n,^2$ is sufficiently large compared with the resonant tank impedance of $\omega_s L_r+1/(\omega_s C_r)$, the equivalent circuit can be redrawn as Fig. 5(b) by exchanging locations of L_m/n^2 and series network of L_r and C_r. Where, ω_s is switching frequency expressed in rad/sec.

Mode 1 ($t_0 \le t < t_1$): When M_8 is turned on at t_0, the secondary current i_s flows through L_r, C_r, M_8, M_6, and transformer secondary side. The primary current i_p increases from zero through the body diode of M_2, the channel of M_3, C_v, and the transformer primary side. From the equivalent circuit in Fig. 5(b), v_{cr} and the primary current referred to the secondary side ni_p can be approximately derived as

$$v_{cr}(t) \approx \left(V_{batt} - \frac{V_{in}}{2n}\right) - \left(V_{batt} + V_{crr} - \frac{V_{in}}{2n}\right)\cos\omega_r(t-t_0) \tag{9}$$

$$ni_p(t) \approx \frac{1}{Z_r}\left(V_{batt} + V_{crr} - \frac{V_{in}}{2n}\right)\sin\omega_r(t-t_0) \tag{10}$$

V_{crr} is the peak voltage of v_{cr} in discharging operation and its expression is as shown in eq. (16). The secondary current i_s is equal to the sum of ni_p and ni_m. When M_8 is turned off, i_s is used to make ZVS condition of M_7.

Mode 2 ($t_1 \le t < t_2$): When M_7 is turned on, mode 2 begins. The power flow is formed as shown in Fig. 4 and i_p begins to decrease. From the equivalent circuit of mode 2, v_{cr} and ni_p can be derived as

$$v_{cr}(t) = -\frac{V_{in}}{2n} + \left(V_{cr}(t_1) + \frac{V_{in}}{2n}\right)\cos\omega_r(t-t_1) + Z_r ni_p(t_1)\sin\omega_r(t-t_1) \tag{11}$$

$$ni_p(t) = -\frac{1}{Z_r}\left(V_{cr}(t_1) + \frac{V_{in}}{2n}\right)\sin\omega_r(t-t_1) + ni_p(t_1)\cos\omega_r(t-t_1) \tag{12}$$

With the similar assumption of mode 2 in charging operation, $ni_p(t_1)$ and $v_{cr}(t_1)$ can be derived from eqs. (9) and (10). They are as follows:

$$v_{cr}(t_1) \cong v_{cr}(D_r T_s) = \left(V_{batt} - \frac{V_{in}}{2n}\right) - \left(V_{batt} + V_{crr} - \frac{V_{in}}{2n}\right)\cos\omega_r D_r T_s \tag{13}$$

$$ni_p(t_1) \cong ni_p(D_r T_s) = \frac{1}{Z_r}\left(V_{batt} + V_{crr} - \frac{V_{in}}{2n}\right)\sin\omega_r D_r T_s \tag{14}$$

Where, D_r is the duty-ratio of M_5 (or M_8) in discharging operation. Mode 2 continues until i_p is decreased to zero and the duration of mode 2 in discharging mode T_{M2r} can be derived as

$$T_{M2r} = \frac{1}{\omega_r}\tan^{-1}\left(\frac{\left(V_{batt} + V_{crr} - \frac{V_{in}}{2n}\right)\sin\omega_r D_r T_s}{V_{batt} - \left(V_{batt} + V_{crr} - \frac{V_{in}}{2n}\right)\cos\omega_r D_r T_s}\right) \tag{15}$$

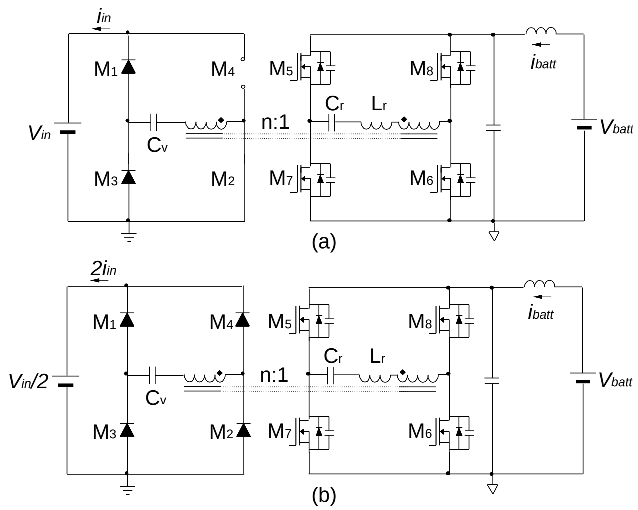

Fig. 6 Equivalent circuit expressed with full-bridge rectifier (b) instead of voltage-doubler rectifier (a)

Mode 3 ($t_2 \le t < t_3$): After mode 2, only the magnetizing current referred to the secondary side ni_m circulates through M_7 and the body diode of M_6. From eqs. (11) and (15), $v_{cr}(t_2)$ can be derived as follows:

$$v_{cr}(t_2) \cong \frac{V_{batt}\left(V_{batt} - \frac{V_{in}}{2n}\right)(1-\cos\omega_r D_r T_s)}{2\left(\frac{V_{in}}{2n}\right) - V_{batt}(1-\cos\omega_r D_r T_s)} \equiv V_{crr} \tag{16}$$

Eq. (16) is the peak value of v_{cr} during discharging operation defined by V_{crr}. When M_6 is turned off, the peak magnetizing current referred to secondary side is used to charge and discharge C_{ds}'s of M_5 and M_6. The first half-cycle comprised of modes 1~3 is charging period of the charge-pump capacitor C_v through the body diode of M_2 and the channel of M_3, and the next half-cycle comprised of modes 4~6 is powering period through the charge-pump capacitor C_v and the body diodes of M_1 and M_3. The two operations are same except for rectifier operation.

D. Input-output relationship of the proposed converter

< Charging operation >

The average input power P_{if} can be calculated by averaging the product of switch current of M_1 (or M_4) and the input voltage V_{in} over half of the switching cycle. Since the magnetizing current is circulating current, it does not contribute to power transfer. Accordingly, P_{if} can be derived with eqs. (2) and (8), which is as follows:

$$P_{if} = \frac{2}{T_s}\int_0^{D_f T_s} V_{in}\frac{i_s(t)}{n}dt = \frac{4C_r V_{in} V_{batt} K_f (V_{in}/n - V_{batt})}{nT_s(2V_{batt} - K_f V_{in}/n)} \tag{17}$$

where, K_f=1−cos$\omega_r D_f T_s$. Since the output power P_{of} is expressed as

$$P_{of} = V_{batt} I_{batt} \tag{18}$$

battery voltage expression according to charging current can be derived as

$$V_{batt} = \frac{4(V_{in}/n)^2 C_r K_f + (V_{in}/n)K_f I_{batt} T_s}{2I_{batt}T_s + 4(V_{in}/n)C_r K_f} \tag{19}$$

This article has been accepted for publication in a future issue of this journal, but has not been fully edited. Content may change prior to final publication. Citation information: DOI 10.1109/TVT.2017.2678532, IEEE Transactions on Vehicular Technology

by equating eq. (17) with eq. (18).

< Discharging operation>

Fig. 6 is the equivalent circuit expressed with full-bridge rectifier instead of voltage-doubler rectifier. The equivalent circuit has exactly same structure with that in charging operation so that the derivation of input-output relationship in discharging operation is same to the case of charging operation. Thus, the results is

$$V_{in} = 2\times\frac{4(nV_{batt})^2(C_r/n^2)K_r + 2(nV_{batt})K_r I_{in} T_s}{4I_{in}T_s + 4(nV_{batt})(C_r/n^2)K_r} \tag{20}$$

where, K_r=1−cos$\omega_r D_r T_s$ and I_{in} is the average input current. Since the discharging control is performed not by I_{in} but by I_{batt} and V_{in} is the constant output voltage regulated by a harmonic regulator, eq. (20) can be rewritten as the following equation:

$$V_{batt} = \frac{V_{in}I_{batt}T_s + (C_r/n)K_r V_{in}^2}{2C_r V_{in} K_r + nI_{batt}T_s K_r} \tag{21}$$

with the condition of $V_{batt}I_{batt}=V_{in}I_{in}$. Eq. (21) gives the information of the minimum battery voltage available at a discharge current command.

III. Design and Control Strategy

The main object of OBC is to charge battery and it has a long operation time of 4~8 hours under full load condition. On the contrary, discharging operation may not occur frequently like charging operation. Thus, main focus of design is to optimize charging operation. To guarantee the charging operation explained in the mode analysis and the soft-switching conditions of power devices, the peak voltage of resonant capacitor should not exceed the battery voltage and the duration from mode 1 to mode 2 should be shorter than half of the switching period. The design procedure has been well explained in reference [26] and it is summarized in section A.

A. Design for charging operation

Since V_{crf} cannot be a negative value, the transformer turns-ratio n should be smaller than $V_{in}/V_{batt,max}$. Also, the maximum operational duty-ratio $D_{f,max}$ should be chosen to secure the duration of mode 3. Using eqs. (7) and (8), and the selected values of $D_{f,max}$ and n, a resonant frequency ω_r can be chosen among the candidates satisfying normal operation conditions of $V_{crf}<V_{batt}$ and $D_fT_s+T_{M2f}<T_s/2$. After then, the resonant capacitor C_r is selected to admit the maximum battery voltage at $D_{f,max}$ and the maximum charging power using eq. (19). The resonant inductor L_r is calculated with the selected C_r. The magnetizing inductance L_m is designed to meet ZVS of upper switches and its guideline is as follows:

$$L_m \le \frac{T_{dead}D_f T_s}{4C_{ds}} \tag{22}$$

It is derived based on the condition that ΔT of the transition time of drain-to-source voltages in switch-bridge is shorter than T_{dead}. To design L_m, it is necessary to select $D_{f,min}$ that is the worst case to accomplish complete ZVS. The designed parameters are verified by checking whether the conditions of $V_{crf}<V_{batt}$ and $D_fT_s+T_{M2f}<T_s/2$ are satisfied under entire battery voltage ranges at maximum charging powers.

B. Control strategy of discharging operation

In discharging operation, the normal operation conditions of $V_{crr}<V_{in}/n$ and $D_rT_s+T_{M2r}<T_s/2$ should be met like charging operation. Using eq. (15), (16), and (21), the minimum discharge voltage satisfying the normal operation conditions can be investigated according to various discharge currents. The result of partial derivatives of eq. (21) according to I_{batt} is

$$\frac{\partial V_{batt}}{\partial I_{batt}} = \frac{C_r T_s V_{in}^2(1-(\cos\omega_r D_r T_s)^2)}{(2C_r V_{in}K_r + nI_{batt}T_s K_r)^2} \tag{23}$$

and it is always positive value, which says that the minimum discharge voltage is increased as discharge current is increased. Therefore, the minimum discharge voltage that can output entire discharge current can be found from the maximum discharge current condition. Unfortunately, the minimum discharge voltage may not meet design specifications because the design parameters are optimized for charging operation. To overcome this problem, another control variable is required to increase the voltage gain for discharging operation. Rearranging eq. (21), it can be written as follows:

$$V_{batt} = \frac{T_s}{K_r}\frac{V_{in}I_{batt}}{2C_r V_{in} + nI_{batt}T_s} + \frac{(C_r/n)V_{in}^2}{2C_r V_{in} + nI_{batt}T_s} \tag{24}$$

The solution of partial derivative of eq. (24) according to T_s is

$$\begin{aligned}\frac{\partial V_{batt}}{\partial T_s} &= \left(\frac{1-\cos\omega_r D_r T_s - \omega_r D_r T_s \sin\omega_r D_r T_s}{(1-\cos\omega_r D_r T_s)^2}\right)\frac{V_{in}I_{batt}}{2C_r V_{in} + nI_{batt}T_s} \\ &+ \frac{T_s}{1-\cos\omega_r D_r T_s}\left(\frac{-nI_{batt}^2 V_{in}}{(2C_r V_{in} + nI_{batt}T_s)^2}\right) - \frac{n(C_r/n)I_{batt}V_{in}^2}{(2C_r V_{in} + nI_{batt}T_s)^2}\end{aligned} \tag{25}$$

As shown in this equation, the slope of battery voltage is influenced by T_s but its sign should be kept constant in order that T_s is used as a control variable. Investigating eq. (25), the slope has negative sign if the following condition is met

$$M \equiv \frac{1-\cos\omega_r D_r T_s - \omega_r D_r T_s \sin\omega_r D_r T_s}{(1-\cos\omega_r D_r T_s)} - \frac{C_r V_{in}(1-\cos\omega_r D_r T_s) + nI_{batt}T_s}{2C_r V_{in} + nI_{batt}T_s} \le 0 \tag{26}$$

To the extent that $\omega_r D_r T_s$ meets eq. (26), the voltage gain of eq. (20) can be additionally increased by increasing T_s regardless of battery current. Therefore, a lower battery voltage can be used for discharging operation.

The minimum battery voltage $V_{batt,min}$ can be calculated using eqs. (15), (16), (21), and $I_{batt,max}$ at a nominal switching frequency. The target minimum battery voltage can be selected with a slightly higher voltage than the calculated minimum battery voltage and the switching frequency is changed to an appropriate value selected among the candidates that satisfy a target minimum battery voltage and eq. (26).

IV. Experimental Results

The prototype charger has been designed with the specifications described in Table 1. The selected devices are listed in Table 2 together with parameters designed with the procedure described in section III. The capacitor C_v is used to prevent the transformer saturation during charging operation and it is also used as charge-pump capacitor having half of the

This article has been accepted for publication in a future issue of this journal, but has not been fully edited. Content may change prior to final publication. Citation information: DOI 10.1109/TVT.2017.2678532, IEEE Transactions on Vehicular Technology

TABLE 1
PROTOTYPE DESIGN SPECIFICATIONS

Items	Specification
Maximum charging/discharging power $P_{o,max}$	6.6kW
Maximum battery current $I_{batt,max}$	20A
Battery voltage V_{batt}	250V~415V
Input voltage V_{in}	400V
Nominal switching frequency f_s	50kHz

TABLE 2
DESIGNED PARAMETERS AND SELECTED DEVICES

Items	Value
Resonant capacitor C_r	400nF
Resonant inductor L_r	35μH
Transformer turns ratio n	0.833
Charge pump capacitor C_v	11μF
Output filter inductor L_f	20μH
Output filter Capacitor C_f	20μF
Magnetizing inductance L_m	250μH
Switch M_1~M_8	IPW65R041CFD×2
Transformer Core	EE6565×2

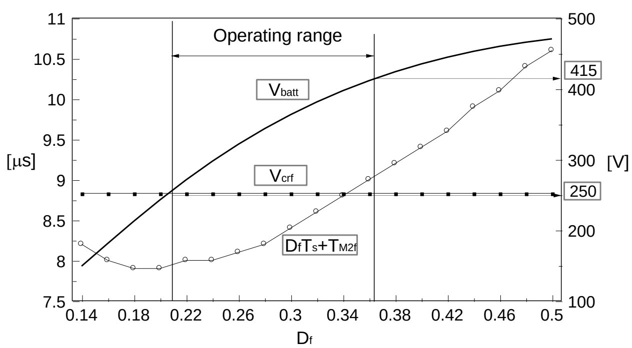

Fig. 7 Plot of V_{crf}, V_{batt}, and $D_fT_s+T_{M2f}$ according to duty-ratio variations at I_{batt}=20A

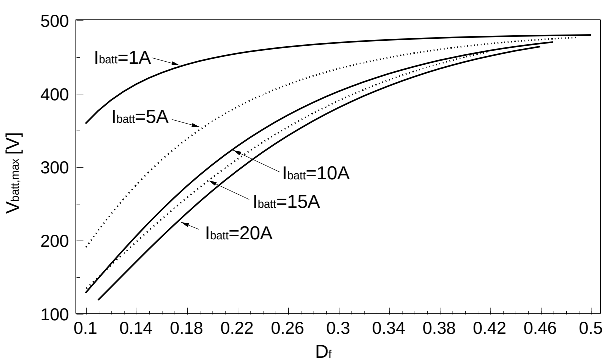

Fig. 8 Maximum charge voltage according duty-ratio and charging

input voltage v_{in}. In addition, resonant frequency formed by C_r and L_r should not be affected by C_v. Considering these roles of C_v, it is better that C_v has a large value, but too large values produce bulky design because high frequency capacitors such as film capacitor are utilized. In this design, a value over 20 times larger than that of resonant capacitor has been chosen for C_v in

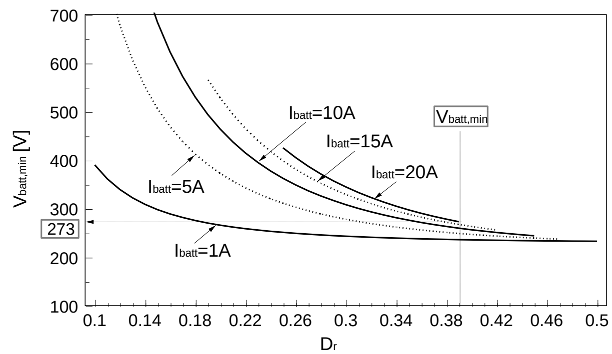

Fig. 9 Minimum discharge voltages according to duty-ratio and discharging current changes under satisfying normal operation conditions

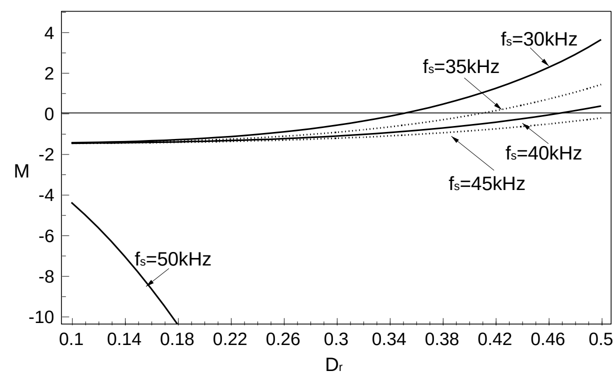

Fig. 10 Index M according to frequency changes at maximum battery current

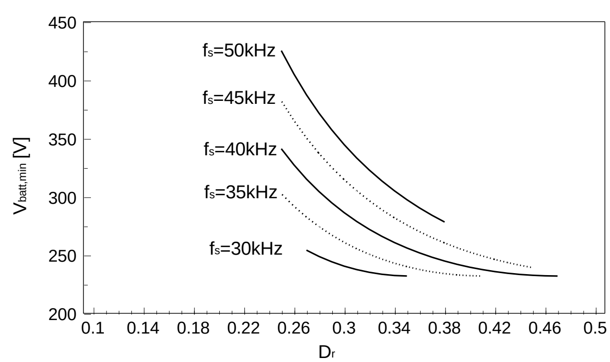

Fig. 11 Minimum discharge voltages according to duty-ratio and switching frequency changes under satisfying normal operating conditions

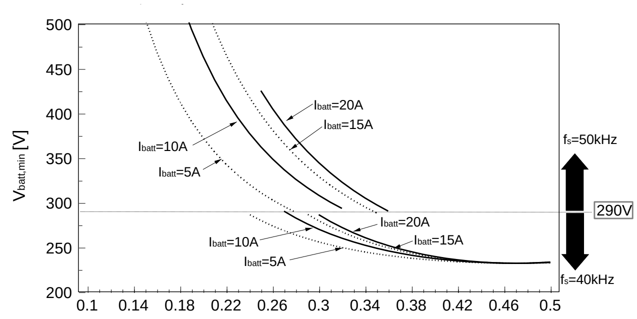

Fig. 12 Minimum discharge voltages according to duty-ratio and switching frequency changes

order that the resonant frequency is determined only by C_r and L_r. As shown in Figs. 7 and 8, this design satisfies the conditions

This article has been accepted for publication in a future issue of this journal, but has not been fully edited. Content may change prior to final publication. Citation information: DOI 10.1109/TVT.2017.2678532, IEEE Transactions on Vehicular Technology

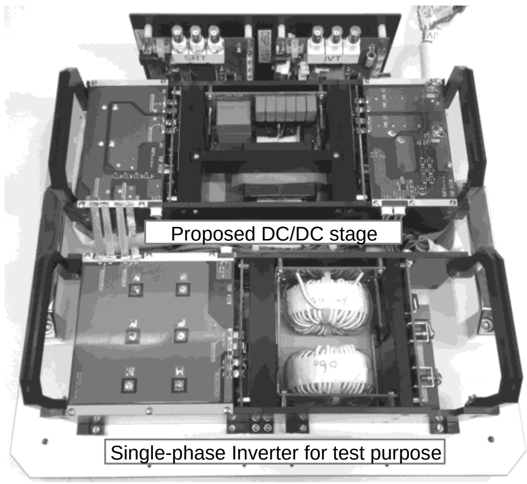

Fig. 13 Implemented prototype

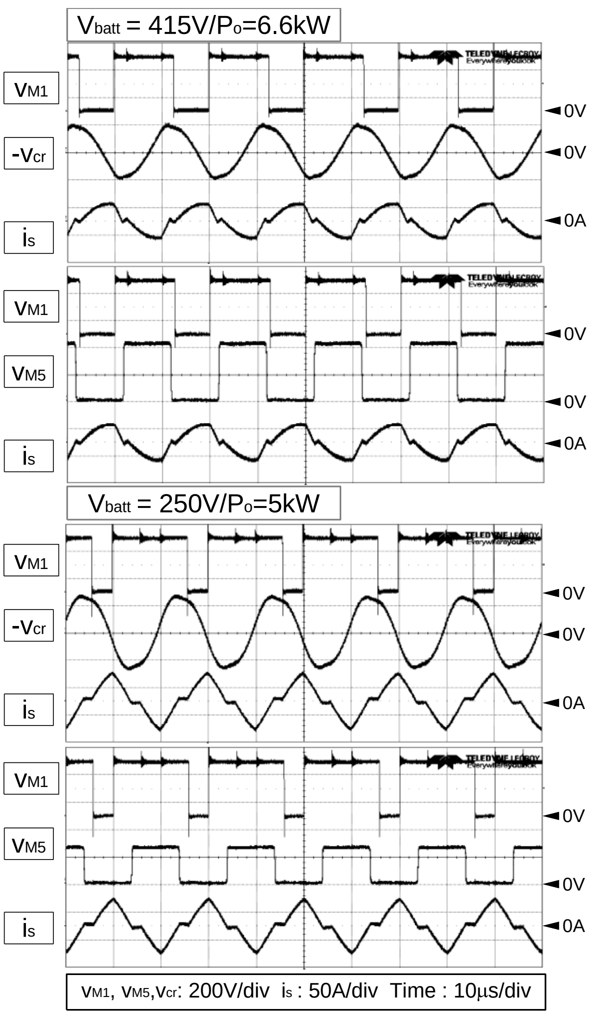

Fig. 14 Measured waveforms in charging operation

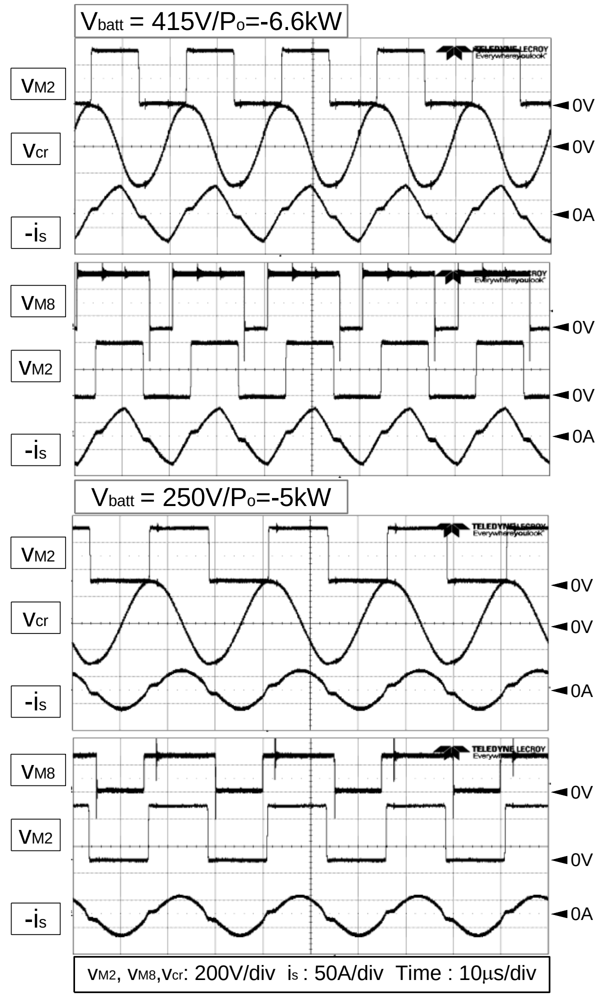

Fig. 15 Measured waveforms in discharging operation

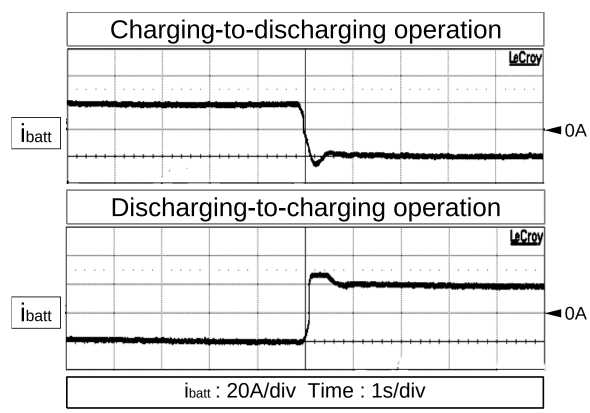

Fig. 16 Transient between charging and discharging operations at V_{batt}=330V

of V_{crf}<V_{batt} and D_fT_s+T_{M2f}<T_s/2 under entire battery voltage ranges at the maximum charging power. Also, the design can deal with entire battery voltage range with normal switching frequency of 50kHz. Fig. 9 is the operational regions satisfying the conditions of V_{crr}<V_{batt} and D_rT_s+T_{M2r}<T_s/2, which are depicted according to discharging current changes. As predicted in eq. (24), it can be seen that the minimum battery discharge voltage becomes high as battery current is increased. The minimum battery voltage, that can operate under all load conditions while satisfying the conditions of V_{crr}<V_{batt} and D_rT_s+T_{M2r}<T_s/2, occurs at 273V. Using eq. (26), the index M can be depicted in Fig. 10 according to frequency changes at the

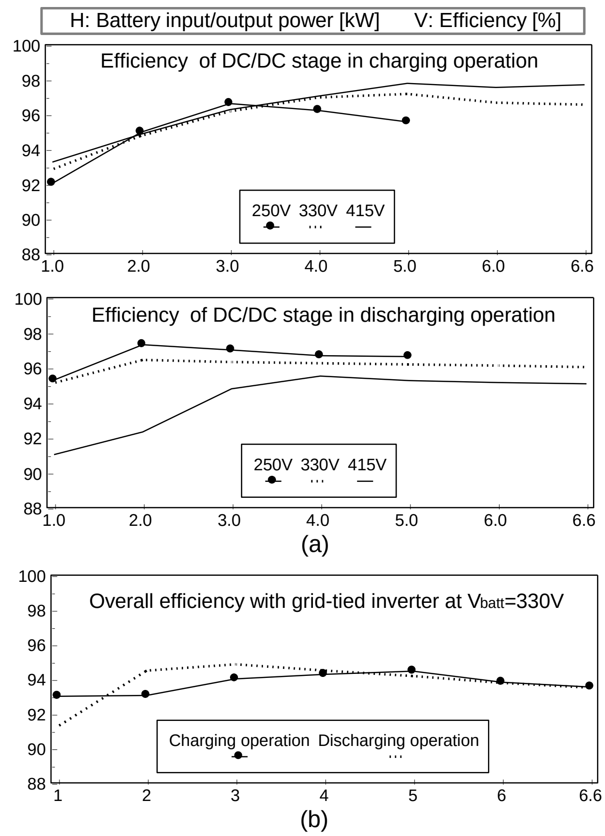

Fig. 17 Measured efficiency according to battery voltages (a) and overall efficiency including single-phase inverter (b)

TABLE 3
PERFORMANCE COMPARISON TABLE

	DAB [24]	CLLLC/CLLC [29]	SRC+GaN [30]	Proposed
Charging power	3.5kW	3.5kW	3.3kW	6.6kW
Switch	IPW041CFD×8	IKW40N65F5×4 FCH041N65F×4	TPH3295WS(GaN)	IPW041CFD×16
Transformer Core	PQ50 type	EE65/32/27-3C95	PQ50/54	EE6565×2
Inductor Core	Additional 70μH	ETD49/25/16-3C95	Integrated	Integrated
Maximum efficiency Upper: Charging operation Lower: Discharging operation	97.5% @330V/3.5kW 97.5% @330V/3.5kW	CLLC: 97.6% @400V/2.25kW 98% @350V/2.45kW CLLLC: 97.6% @400V/2.25kW 97.8% @400V/2.25kW	97.3% @350V/3.5kW 97.2% @350V/3.5kW	97.7% @413V/6.6kW 97.3% @250V/2kW
Control method	Variable frequency/variable duty-ratio	Variable frequency	Variable frequency	Fixed frequency (only one frequency change at low battery voltage during discharging operation)

maximum battery current. For example, D_r less than 0.47 can be used at f_s=40kHz. Fig. 11 is the minimum discharge battery voltage satisfying the conditions of $V_{crr}<V_{batt}$ and $D_rT_s+T_{M2r}<T_s/2$. It is depicted using eq. (15), (16), and (21) at the maximum battery current according to duty-ratio of discharging operation and switching frequency changes. Duty-ratio ranges according to switching frequency changes in Fig. 11 are included in negative *M* in Fig. 10. Accordingly, the switching frequencies depicted in Fig. 11 can be used for another control variable. At the nominal switching frequency of 50kHz, the minimum battery voltage capable of flowing entire discharging current is about 273V and frequency changing voltage should be selected above this voltage. In this design, we have selected 290V considering a margin and 40kHz has been selected at which the lowest battery voltage is available. The resulting minimum discharge voltage can be depicted in Fig. 12. Fig. 13 is the implemented prototype bidirectional charger comprised of the proposed converter and single-phase inverter for test use. The controller shown in Fig. 1 was implemented with DSP TMS320F28335. Figs. 14 and 15 are switching waveforms measured according to power flow directions. From these figures and eqs. (2) and (10), it can be seen that the more the battery voltage is decreased, the higher the peak value of transformer current at switching instant occurs during charging operation. Accordingly, a high switching loss happens at a low battery voltage and the switching loss becomes worse at a high output power so that the efficiency degradation is likely to occur at a low battery voltage and a high output power. On the other hand, the peak value of transformer current happens at a high battery voltage during discharging operation so that high switching loss occurs at the high battery voltage. Also, the nominal switching frequency of 50kHz can accommodate the entire battery voltage range during charging operation, but switching frequency is changed to 40kHz at lower battery voltage during discharging operation. Fig. 16 shows the transient between charging and discharging operations. It shows that the transition times are not fast because the proposed method has the selective bidirectional operation dominated by external power flow commands. Fig. 17(a) is the measured efficiency according to battery voltages, which includes driving power consumption, controller power consumption, and output filter loss. In charging operation, 97.2% has been recorded at 330V/6.6kW and the maximum efficiency of 97.8% is measured at 415V/6.6kW. On the other hand, 96.2% has been recorded at 330V/6.6kW and the maximum efficiency of 96.8% is measured at 250V/5kW in discharging operation. Overall efficiency including single-phase inverter is as shown in Fig. 17(b). Table 3 shows the performance comparisons between the proposed charger and recently reported topologies. It shows that it is not inferior to recent works in the aspect of structure and efficiency despite that the proposed converter mainly uses constant frequency control.

V. CONCLUSIONS

An isolated/bidirectional PWM-RC has been suggested for bidirectional OBCs. Using the structure change method, the proposed charger can be operated under bidirectional power flow by overcoming gain characteristic which has always ‘buck type’ operation regardless of power flow directions. Analysis has been performed to derive the voltage gain and the design

This article has been accepted for publication in a future issue of this journal, but has not been fully edited. Content may change prior to final publication. Citation information: DOI 10.1109/TVT.2017.2678532, IEEE Transactions on Vehicular Technology

equations, and an additional control technique to increase the converter gain has been proposed based on the analysis. To verify the performances, a 6.6KW prototype charger has been implemented with the design guidelines. Experimental results show that 97.2% has been recorded at 330V/6.6kW in charging operation and 96.2% has been recorded at the same condition in discharging operation. Therefore, it may be another candidate for DC/DC stage in V2G(H) EV chargers or backup power supplies such as emergency power system and household energy storage system.

REFERENCES

[1] M. C. Kisacikoglu, B. Ozpineci, and L. M. Tolbert, “EV/PHEV Bidirectional Charger Assessment for V2G Reactive Power Operation,” *IEEE Trans. Power Electron.*, vol. 28, no. 12, pp. 5717-5727, Dec. 2013.

[2] V. Monteiro, B. Exposwto, J. G. Pinto, R. Almeda,J. C. Ferreira, A. A. N. Melendez, and J. L. Afonson, “On-Board Electric Vehicle Battery Charger with Enhanced V2H Operation Mode,” in *Proc. IEEE IECON*, 2014, pp. 1636-1642.

[3] R. J. Ferreira, L. M. Miranda, R. E. Araujo, and J. P. Lopez, “A New Bi-Directional Charger for Vehicle-to-Grid Integration,” in *Proc. IEEE PES ISGTEurope*, 2011, pp. 1-5.

[4] J. G. Pinto, V. Monteiro, H. Goncalnas, and J. L. Afonso, “Onboard Reconfigurable Battery Charger for Electric Vehicles With Traction-to-Auxiliary Mode,” *IEEE Trans. Veh. Techol.*, vol. 63, no. 3, pp. 1104-1116, Mar. 2014.

[5] D. C. Erb, O. C. Onar, and A. Khaligh, “Bi-directional Charging Topologies for Plug-In Hybrid Electric Vehicles,” in *Proc. IEEE APEC*, 2010, pp. 2066-2072.

[6] M. Yilmaz and P. T. Krein, “Review of Battery Charger Topologies, Charging Power Levels, and Infrastructure for Plug-In Electric and Hybrid Vehicles,” *IEEE Trans. Power Electron.*, vol. 28, no. 5, pp. 2151-2169, May 2013.

[7] B.Singh, B. N. Singh, A. Chandra, K. Al-Haddad, A. Pandey, and D. P. Kothari, “A Review of Three-Phase Improved Power Quality AC–DC Converters,” *IEEE Trans. Ind. Electron.*, vol. 51, no. 3, pp. 641-660, Jun. 2004.

[8] B.Singh, B. N. Singh, A. Chandra, K. Al-Haddad, A. Pandey, and D. P. Kothari, “A Review of Single-Phase Improved Power Quality AC–DC Converters,” *IEEE Trans. Ind. Electron.*, vol. 50, no. 5, pp. 962-981, Oct. 2003.

[9] H. Zhang, L. M. Tobert, J. H. Han, M. S. Chinthavali, and F. Barlow, “18 kW Three Phase Inverter System Using Hermetically Sealed SiC Phase-Leg Power Modules,” in *Proc. IEEE APEC* , 2010, pp. 1108-1112.

[10] M. Chinthavali, C. Ayers, S. Campbell, R. Wiles, and B. Ozpineci, “A 10-kW SiC Inverter with A Novel Printed Metal Power Module With Integrated Cooling Using Additive Manufacturing,” in *Proc. IEEE WiPDA*, 2014, pp. 48-54.

[11] E. Gurpinar and A. Castellazzi, ”Single-Phase T-Type Inverter Performance Benchmark Using Si IGBTs, SiC MOSFETs, and GaN HEMTs,” *IEEE Trans. Power Electron.*, vol. 31, no. 10, pp. 7148-7160, Oct. 2016.

[12] A. Yamane, K. Koyanagi, M. Kozako, K. Fuji, and M. Hikita, “Fabrication and Evaluation of SiC Inverter Using SiC-MOSFET,” in *Proc. IEEE PEDS*, 2013, pp. 1029-1032.

[13] S. Yin, K. J. Tseng, C. F. Tong, R. Simanjorang, C. J. Gajanayake, A. Gupta, “A 99% efficiency SiC three-phase inverter using synchronous rectification,” in *Proc. IEEE APEC*, 2016, pp. 2942-2949.

[14] A. Khaligh and S. Dusmez, “Comprehensive Topological Analysis of Conductive and Inductive Charging Solutions for Plug-In Electric Vehicles,” *IEEE Trans. Veh. Techol.*, vol. 61, no. 8, pp. 3475-3488, Oct. 2012.

[15] M. Adedi, B. M. Song, and R. Y. Kim, “Nonlinear-Model Predictive Control Based Bidirectional Converter for V2G Battery Charger Applications,” in *Proc. IEEE VPPC*, 2011, pp. 1-6.

[16] T. F. Wu, J. G. Yang, C. L. Kuo, K. H. Sun, and Y. K. Chen, “Comparison of Bi-directional Isolated Full-bridge Converters with Combinations of Active and Passive Snubbers,” in *Proc. IEEE ECCE*, 2011, pp. 127-133.

[17] J. H. Jegal, Y. S. Noh, and C. Y. Won, “Control Method for Increasing Efficiency of Current-fed Isolated Bi-directional Dual Half-bridge Converter using Resonant Switch,” in *Proc. IEEE ITEC-AP*, 2016, pp. 302-307.

[18] L. Zhu, “A Novel Soft-Commutating Isolated Boost Full-Bridge ZVS-PWM DC–DC Converter for Bidirectional High Power Applications,” *IEEE Trans. Power Electron.*, vol. 21, no. 2, pp. 422-429, Mar. 2006.

[19] E. V. de Souza and I. Barbi, “Bidirectional Current-Fed Flyback-Push-Pull DC-DC Converter,” in *Proc. BPEC*, 2011, pp. 8-13.

[20] A. Mehdipour and S. Farhangi, “Comparison of Three Isolated Bi-directional DC/DC Converter Topologies for a Backup Photovoltaic Application,” in *Proc. EPECS*, 2011, pp. 1-5.

[21] R. W. De Doncker, D. M. Divan, and M. H. Kheraluwala, “A Three-phase Soft-Switched High-Power-Density dc/dc Converter for High-Power Applications,” in *Proc. IAS*, 1988, pp. 796-805.

[22] R. P. Twiname, D. J. Thrimawithana, U. K. Madawala, and C. Baguley, “A Resonant Bi-Directional DC-DC Converter,” in *Proc. IEEE ICIT*, 2014, pp. 307-311.

[23] A. K. Jain and R. Ayyanar, “PWM Control of Dual Active Bridge: Comprehensive Analysis and Experimental Verification,” *IEEE Trans. Power Electron.*, vol. 26, no. 4, pp. 1215-1227, Apr. 2011.

[24] G. Liu, D. Li, J. Q. Zjang, and M. L. Jia, “High Efficiency Wide Range Bidirectional DC/DC Converter for OBCM Application,” in *Proc. PEAC*, 2014, pp. 1434-1438.

[25] J. Kan, Y. Wu, Y. Tang, B. Zhang, and Z. Zhang, “Dual Active Full-bridge Bidirectional Converter for V2G Charger Based on High-frequency AC Buck-boost Control Strategy,” in *Proc. IEEE ITEC-AP*, 2016, pp. 46-50.

[26] B. J. Byen, K. P. Kang, Y. H. Cho, and A. N. Yoo, “A High Efficiency Variable Modulation Strategy for a Dual-Active-Bridge Converter with a Wide Operating Range,” in *Proc. ICPE*, 2015, pp. 240-245.

[27] B. K. Lee, J. P. Kim, S. K. Kim, and J. Y. Lee, “A PWM SRT DC/DC Converter for 6.6-kW EV Onboard Charger,” *IEEE Trans. Ind. Electron.*, vol. 63, no. 2, pp. 894-902, Feb. 2016.

[28] H. Kato H. Matsuo, Y. Sakamoto, and M. Nakaishi, “Novel series resonance DC-DC converter with voltage doubler rectifier,” in *Proc. IEEE ICSET*, 2010, pp. 1-6.

[29] Z. U. Zahid, Z. M. Dalala, R. Chen, B. Chen, and J. S. Lai, “Design of Bidirectional DC–DC Resonant Converter for Vehicle-to-Grid (V2G) Applications,” *IEEE Trans. Transp. Electrif.*, vol. 1, no. 3, pp. 232-244, Oct. 2015.

[30] G. Liu, D. Yi, Y. Jang, aand J. Zhang, “Over 300kHz GaN Device Based Resonant Bidirectional DCDC Converter with Integrated Magnetics,” in *Proc. IEEE APEC*, 2016, pp. 595-600.

Byung-Kwon Lee was born in cheonan-si, Republic of Korea, in 1987. He received his B.S. degrees in Electrical Engineering from Myongji University, Young-in, in 2011, respectively. Since 2012, he is pursuing the Ph.D. degree in electrical engineering through the combined M.S./Ph.D degree program at Myongji University. His current research interests are in the areas of power electronics application which include dc/dc bi-directional converter, ac/dc PFC converter, and battery charger.

Jong-Pil Kim received the B.S. degree in Electrical Engineering from Soongsil University, Seoul, Korea, in 2005. From 2005 to 2010, he worked as a Manager in Power Advanced Development Group, Samsung Electro-Mechanics. Since 2011, he is working at Advanced Eco-Vehicle Development Team, Hyundai Motors. His research interests are in the areas of power electronics which include on-bard battery charger, low-voltage DC/DC converter, and bidirectional converter for vehicle driving PCU.

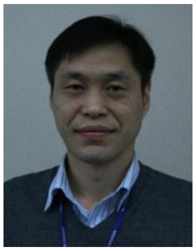

Sam-Gyun Kim received his B.S. degree in Mechanical Engineering from Korea Advanced Institute of Science and Technology, Taejon, Korea, in 1991 and joined Hyundai Motor Co. in 1994. He is currently working at Advanced Eco-Vehicle Development Team. His research interests are motor design and power conversion circuits for vehicle driving PCU which include on-bard battery charger, low-voltage DC/DC converter, bidirectional converter, and inverter.

Jun-Young Lee (M'12) received his B.S. degree in Electrical Engineering from Korea University, Seoul, in 1993 and his M.S. and Ph.D. degrees in Electrical Engineering from Korea Advanced Institute of Science and Technology, Taejon, Korea, in 1996 and 2001, respectively. From 2001 to 2005, he worked as a Manager in Plasma Display Panel Development Group, Samsung SDI where he was involved in circuit and product development. From 2005 to 2008, he worked as a faculty member in the School of Electronics and Computer Engineering, Dankook University. In 2008, he joined the School of Electrical Engineering, Myongji University, as an associate professor. His research interests are in the areas of power electronics which include converter topology design, soft switching techniques, display driving system, and battery charger system.